THE ASTROPHYSICAL JOURNAL, 419:66–77, 1993 December 10

SPATIALLY RESOLVED X-RAY SPECTROSCOPY OF THE MERGING GALAXY CLUSTER A2256

T. MIYAJI[1], R. F. MUSHOTZKY, M. LOEWENSTEIN,[2] P. J. SERLEMITSOS, F. E. MARSHALL, R. PETRE,
K. M. JAHODA, E. A. BOLDT, S. S. HOLT, J. SWANK, A. E. SZYMKOWIAK, AND R. KELLEY
Laboratory for High-Energy Astrophyics, NASA/Goddard Space Flight Center, Greenbelt, MD 20771
Received 1992 October 12; accepted 1993 June 21

ABSTRACT

The cluster of galaxies A2256 was observed with BBXRT (Broad Band X-ray Telescope) during the Astro 1 mission with a total exposure of ~4000 s. Moderate resolution spectra of parts of this cluster of galaxies give information complementary to the high spatial resolution observation of the same cluster by *ROSAT*. *ROSAT* spectral images (Briel et al.) have shown evidence of a merger with the northwest clump being cooler than the main cluster body. The BBXRT spectra also show an indication of a lower temperature [$kT = 4.6(+0.9, -0.7)$ keV, 90% confidence errors] in the same general area. The BBXRT data from other regions within 10′ from the center show temperatures ($T \sim 7$ keV) consistent with the *Ginga* overall average and constrain the temperature gradient by limiting the polytropic index to $\gamma = 1.10 \pm 0.35$ (90% confidence errors).

We have detected absorption in excess of the galactic value in several regions of the cluster, similar to that seen in other clusters with the *Einstein* SSS. One of the observed regions shows an apparent oxygen edge absorption feature at $0.54 \lesssim E_{\rm edge} \lesssim 0.62$ keV with an edge optical depth of the order of unity. This range of edge energy corresponds to absorption by oxygen with ionization stage between O^{2+} and O^{4+}. This suggests the existence of about 10^{12}–10^{13} $M_\odot$ of warm ($T \sim 0.5$–5×10^5 K) absorbing gas. It is unlikely that this component has its origin in the hot intracluster gas, compressed by the shock waves generated in the cluster merging and subsequently cooled, because the cooling timescale of the postshock gas is too large. It may have originated from the cold gas in the subcluster cooling flow heated up by shock waves or ionized by radiation sources.

Using spatially resolved temperature information and absolute fluxes from the BBXRT data, along with core radius and the β-parameter of the modified King profile from the *ROSAT* PSPC data, we have obtained radial mass profiles of the X-ray emitting gas and the total gravitational mass. At $r \sim 0.8$ h_{50}^{-1} Mpc, the binding mass range is ~2.8–3.7 $\times 10^{14}$ $M_\odot$ for a range of models consistent with the BBXRT spectral data. This gives a total mass within ~0.8 Mpc of about 5 times the mass of X-ray emitting gas. The total mass and gas fraction of the inner 1 Mpc of the cluster are very similar to those of the Coma Cluster.

Subject headings: cooling flows — galaxies: clusters: individual (A2256) — galaxies: interactions — intergalactic medium — X-rays: galaxies

1. INTRODUCTION

X-ray emission from clusters of galaxies primarily comes from thermal bremsstrahlung emission from a hot, thin plasma embedded in the gravitational potential well of the cluster. X-ray images of clusters of galaxies with the *Einstein* IPC (Forman & Jones 1990; Davis & Mushotzky 1992) and the *ROSAT* PSPC (Böhringer et al. 1992) have revealed that many of them have significant substructures. Such substructures are also seen in the distribution of galaxies in clusters (Geller & Beers 1982; Beers & Geller 1983). Numerical simulations including N-body particles and hydrodynamic gas by Evrard (1990a, b) Thomas & Couchman (1992), and Schindler & Müeller (1993) give direct comparisons with X-ray observations, and show that merging of clusters can be seen as substructures in the X-ray images. Cluster mergings are commonly seen in these simulations, based on the framework of a cold dark matter (CDM) universe (see also Richstone, Loeb, & Turner 1992), and these mergings appear as substructures in X-ray images.

The *ROSAT* PSPC revealed an example of substructure characteristic of such a merging event in the rich cluster of galaxies A2256 (Briel et al. 1991, hereafter B91). Its double-peaked structure can be modeled by a spherically symmetric main body with $kT \sim 10$ keV and a small clump with $kT \sim 2$ keV. A detailed analysis of the *Einstein* IPC image by Davis & Mushotzky (1993), fitting the surface brightness profile with an elliptical main body and substructures, found a similar clump and a point source–like peak. Optical observations of member galaxies show that radial velocities of galaxies in this cooler clump are ~2100 km s^{-1} less than the main cluster body (B91). These observations indicate that A2256 is undergoing a merging event of two clusters of galaxies.

Azimuthally averaged X-ray surface brightness profiles of *Einstein* IPC images of clusters of galaxies show that many are well fitted by a modified King profile (Jones & Forman 1984). Fitting the surface brightness with this form allows an analytic estimate of the mass of the X-ray emitting gas in the cluster. With the assumption of hydrostatic equilibrium, this profile, with spatially resolved temperature data, can also yield the total binding mass of the cluster inside a certain radius and one can measure the amount and the distribution of dark matter in the cluster. For higher temperature clusters such as Coma and A2256, lack of spatially resolved temperature data caused large uncertainties in the binding mass estimates (e.g., Fabricant, Rybicki, & Gorenstein 1984, hereafter FRG) from this kind of analysis. For lower temperature clusters, the rough spectral

[1] Also Department of Astronomy, University of Maryland.
[2] Also Universities Space Research Association.

resolution of the *Einstein* IPC was sufficient to set some limits on the temperature gradient term of the binding mass estimate (Fabricant & Gorenstein 1983; Matilsky, Jones, & Forman 1985). Some effort has been made to constrain the temperature gradient for the Coma Cluster by comparing temperature measurements from a few instruments with different fields of view (Hughes 1989) or from an observation with a coded mask telescope (Watt et al. 1992). While these techniques can be applied to a cluster as close as Coma, data from an instrument providing higher spatial resolution temperature measurement were needed to give information about the temperature gradient of A2256, which is 2.5 times farther away.

High spatial resolution X-ray images of clusters reveal important characteristics such as substructures and significant information on mass profiles, while the X-ray spectra of the intracluster gas contains information on the gas temperature, heavy-element abundances, and amount of absorbing material along the line of sight. One of the important discoveries about galaxy clusters with a high spectral resolution experiment was reported by White et al. (1991). They found absorption in excess of the absorption due to our Galaxy in many cooling flow clusters with the moderate spectral resolution of the *Einstein* SSS (Solid State Spectrometer). This implies that a large amount ($\sim 10^{12}$–10^{13} $M_\odot$) of cold material resides in the cooling flow regions.

The Broad Band X-ray Telescope (BBXRT, Serlemitsos et al. 1992) on the Astro 1 mission provided a unique opportunity to obtain high-quality spectra of clusters of galaxies over a band of 0.3–10 keV with some positional sensitivity. Each of its twin telescopes has a set of five lithium-doped silicon (Si-Li) detectors, one surrounded by the others as seen in Figure 1. In this paper, we report the results of the BBXRT observation of the galaxy cluster A2256 utilizing the spectral resolution and positional sensitivity of the instrument. In § 2, we describe observations of A2256 with BBXRT. In § 3, we present the results of the spectral fits to the data. The detection of extra absorption, probably the photoabsorption edge of partially ionized oxygen, is also reported here. In § 4, we describe the surface brightness and temperature profile fits using the spatially resolved data of BBXRT. Results are discussed in § 5. At the redshift of A2256 ($z = 0.058$, Fabricant, Kent, & Kurtz 1989), a minute of arc corresponds to a projected distance of $0.10\, h_{50}^{-1}$ Mpc ($H_0 = 50\, h_{50}$ km s^{-1} Mpc^{-1}).

2. OBSERVATIONS

A2256 was observed with BBXRT on day 5 and day 8 of the Space Shuttle Mission Astro 1 (STS-35) launched on 1990 December 2. X-ray photons were focused on the focal plane of each of the two X-ray telescopes (named the A and B telescopes). Five pixels of the detector are placed at the focal plane of each telescope, one at the center (namely A0/B0) surrounded by the other four outer pixels (A1–A4/B1–B4). Figure 1 shows the detector configuration projected on the sky together with the slight misalignment of the optical axes of the two telescopes. Photons entering each pixel were counted in corresponding pulse height channels to produce energy spectra. The energy resolution was ~100 eV at 1 keV (noise limited) and ~150 eV at 6 keV. The total exposure for A2256 was about 4000 s. Exposures on A2256 were obtained during orbit nights and problems arising from contamination by airglow were not important.

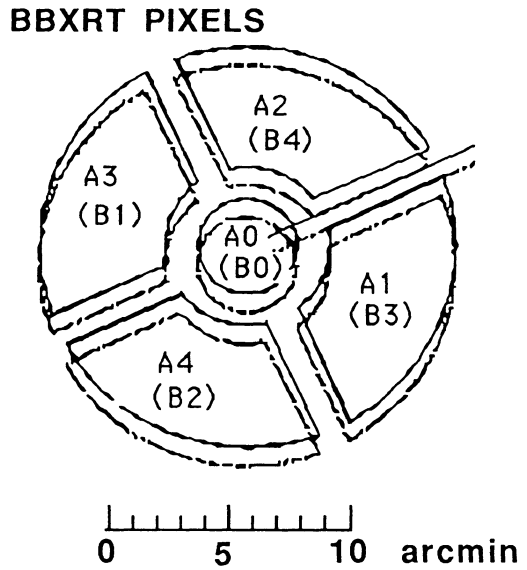

FIG. 1.—BBXRT pixel configurations projected on the sky. The ones shifted slightly downward signifiy the B pixels. The A1/A2 (B3/B4) border is shown by a tick to specify the orientation of the detector.

An aspect camera attached to the BBXRT was used to monitor the pointing direction of the telescopes, providing an aspect solution, as a function of time. During each of the day 5 and day 8 exposures, there were two pointing positions separated by ~5′ and ~2′, respectively. Typical rms fluctuations of the aspect solutions for a given pointing are about 0.′1 with a possible systematic error of $\lesssim$0.′2. The log of A2256

TABLE 1

LOG OF OBSERVATIONS

Observation Number	Start MET[a] (day-hr:min)	Exposure (s)	Aspect Solutions[b] (degrees, 1950.0) R.A.	Decl.	Rotation	Net Source Count Rates (0.8–10 keV) (counts s^{-1}) A0	A1	A2	A3	A4	B0	B1	B2	B3	B4
1.....	5-3:13	1099	257.27	78.68	200	0.14	0.75	0.34	...	...	0.07	...	...	0.49	0.33
2.....	5-3:35	821	257.15	78.75	197	0.13	0.92	...	...	...	0.10	...	...	0.72	0.12
3.....	8-4:26	518	256.95	78.70	218	0.40	0.43	0.49	0.23	...	0.31	0.18	...	0.40	0.51
4.....	8-4:40	1116	256.77	78.72	218										

[a] MET (Mission Elapsed Time) 0.0 = day 336.284039 of 1990, equals JD 2,448,227.784039.

[b] Aspect solution is the position of the sky corresponding to the center of the A0 pixel derived from the aspect camera. A zero rotation corresponds to the case where the A4 pixel is at the north of the central pixel on the sky and positive value corresponds to clockwise rotation.

[c] Count rates correspond to the background-subtracted net count rates for the observations for pulse height channels roughly corresponding to the X-ray photon energy range of 0.8–10 keV. Count rates are shown only for those used in analysis. The count rates on the no. 3 line are for the total counts from no. 3 and no. 4. There is a shift period of 197 s between no. 1 and no. 2. The data from the shift period were also added when data from no. 1 and no. 2 were added.

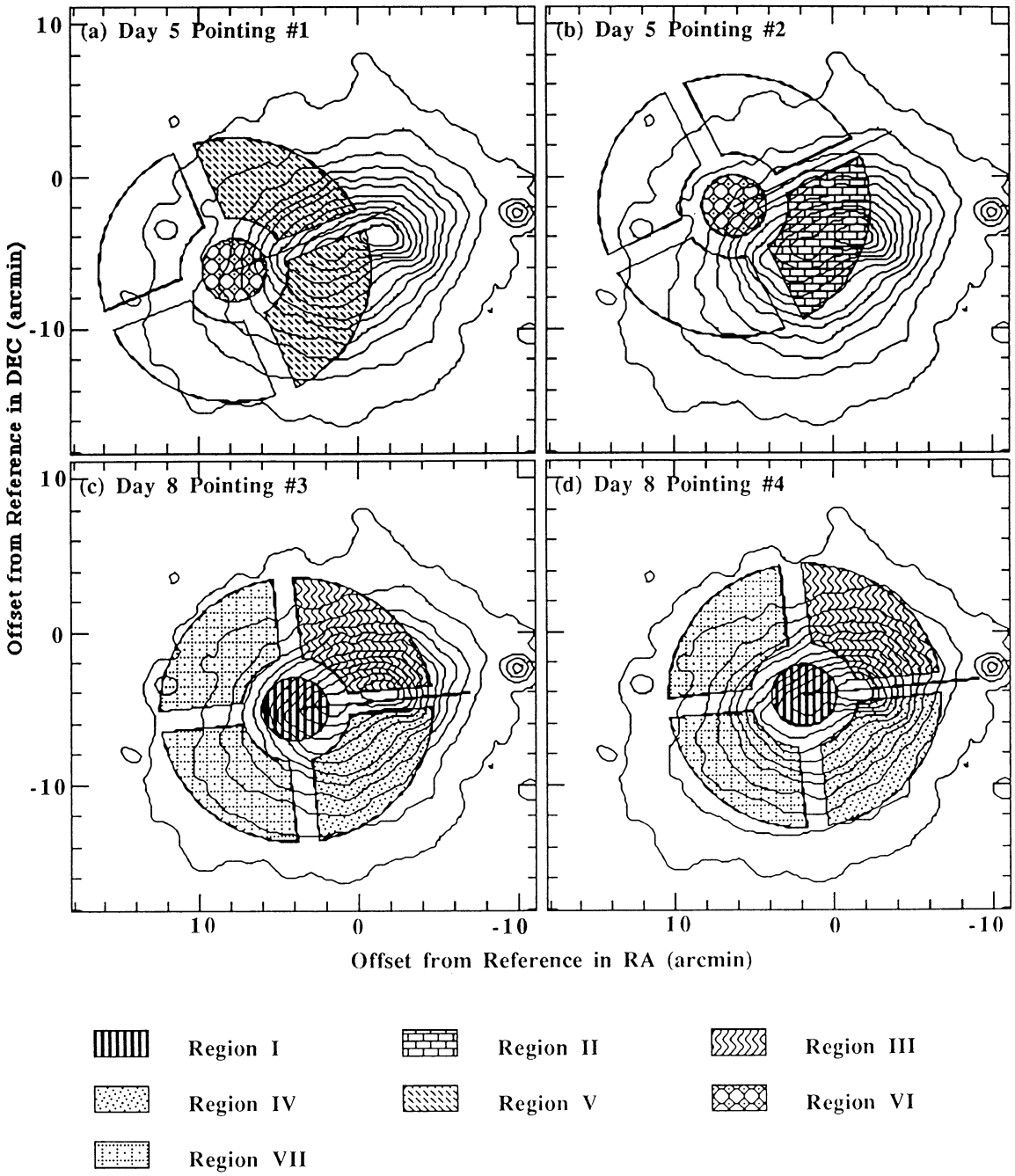

FIG. 2.—(*a*)–(*d*) The BBXRT pointings are shown following the convention in Fig. 1 based on the aspect solutions for pointings 1–4 in Table 1. Only A pixels are drawn. The underlying contour represents the X-ray surface brightness distribution of the *ROSAT* PSPC image. The contour levels are 5, 10, 15, 20, 30, 40, 50, 60, 70, 80, and 90% of the peak count in the image. The reference point is R.A. = $17^h06^m30^s$, decl. = 78°47′10″ (1950). The groupings (see Table 2) for spectral fits are shown by different screen tones as indicated.

observations is shown in Table 1 along with the net source count rates over channels roughly corresponding to photon energies between 0.8 and 10 keV. The pixels which were not included in the analysis usually have less than 3 σ detections over this channel range and/or the electrical noise is so high that it affects the spectral analysis. Figure 2 shows the BBXRT pixels projected on the contour map of the *ROSAT* PSPC image of A2256 for the four pointings in Table 1. The point spread function (PSF) of BBXRT is larger than that of the underlying image and has a HPR (half-power-radius) of $\sim 1'.7$.

3. SPECTRAL ANALYSIS

3.1. *General Procedure*

Spectral fits were performed using the XSPEC package (Shafer, Haberl, & Arnaud 1989). We have used either the minimum χ^2 or the maximum likelihood statistics for analysis as discussed in § 3.2 and 3.3. The system response matrices depend on the position of the object on the focal plane as well as characteristics of individual pixels. Off-axis angle dependence of the response, mainly due to the angular dependence of

the energy-dependent vignetting, has been modeled and an appropriate procedure to create a response matrix as a function of the off-axis angle of the source has been established (Weaver 1993). For an extended object like A2256, we used a single off-axis angle (6′) in generating the response matrices for outer pixels and on-axis response matrices were used for the central pixels. This was always within 1′ of the flux-averaged off-axis angle of the portion of the template image (the *ROSAT* PSPC image) which falls into a given outer pixel used for the analysis. A 1′–3′ change in generating the response matrix did not change the results. In order to justify the use of the single off-axis angle response, a fake pulse height spectrum was generated as a weighted sum of two sets of pulse height data of a 7 keV Raymond-Smith spectrum, one generated with the 7.5 off-axis angle response and the other, given the half weight of the previous one, with the 3′ off-axis response. Then the fake pulse height spectra were fitted with the 6′ off-axis response. The fit gave 6.9 keV, which deviates from the true temperature by only a small fraction of the statistical error.

The pulse height spectra obtained separately for four pointings and pixels are grouped according to their positions on the sky (regions I–VII). Spectra from the same region are usually fitted together by co-adding the pulse height spectra channel by channel (if they are from the same detector pixels or from pixels with responses considered nearly identical) and by making use of the simultaneous fitting capabilities of the XSPEC package. Figure 2 shows the pixels belonging to regions I–VII. Table 2 also shows, for each region, its effective radius ($R_{\rm eff}$), i.e., the *Einstein* IPC flux (Harris et al. 1990) averaged distance from the cluster center of the region, and the radius range in which 80% of the IPC flux falls.

Background pulse height spectra were collected from the night-time blank-sky observations with the same ranges of the "Guard-A rate," an indicator of the charged particle background that varies roughly proportional to the internal background (Weaver 1993), as the corresponding observations such that the mean guard rate is about the mean value for the observation (within ~5%). The guard-A rate varied by about 20% during the day 8 observations and about 40% in the day 5 observations. In any case, the flux from A2256 was such that a 20% change in the assumed background level does not change the results significantly. The energy lower bounds for the analysis were determined based on the background levels and the energy range for each pixel where the calibration is reliable.

TABLE 2

REGIONS FOR THE BBXRT ANALYSIS

Region	Pointing-Pixel[a] Combinations	$R_{\rm eff}$[b]	Radius Range[b]
I	(3A0 + 4A0) & (3B0 + 4B0)	2.0	0.7–3.5
II	2A1 & 2B3	2.4	0.9–4.0
III	3A2 + 4A2	4.3	2.0–6.8
IV	(3A1 + 4A1) & (3B3 + 4B3)	5.4	3.4–7.6
V	(1A1 + 1A2) & (1B3 + 1B4)	3.9	1.5–6.9
VI	(1A0 + 2A0) & (1B0 + 2B0)	6.0	4.2–8.0
VII	(3A3 + 4A3) & (3B1 + 4B1) & (3B2 + 4B2)	6.9	4.7–9.4

[a] A pulse height spectrum is signified by a combination of a pointing no. (Table 1) and a pixel name (Fig. 1). A "+" symbol indicates an addition of pulse height spectra and an "&" symbol indicates a simultaneous fitting. If pulse height spectra from no. 1 and no. 2 pointings are added for the same pixel, the spectrum from the corresponding shifting period (see caption in Table 1) is also added.

[b] See text for definitions of $R_{\rm eff}$ and the Radius Range.

TABLE 3

FIT TO THE COMBINED INNER REGION

Parameter	Value (90% confidence Errors)
Temperature	$6.6 + (1.1; -0.8)$ keV
Abundance (cosmic = 1)	0.40 ± 0.21
$N_{\rm H}$	$(1.1 \pm 0.3) \times 10^{21}$ cm^{-2}
χ^2/d.o.f.	197/180

In particular, we excluded the lowest energy channels if the background level, which rises rapidly with decreasing pulse height channel, is more than about half of the source flux level.

3.2. *The Combined Inner Region*

In order to give strict constraints on temperature and heavy-element abundance of the cluster from the available data, we have made a combined analysis of regions II, IV, and V. Region III was not included because it is significantly contaminated by the cool clump. Regions I, VI, and VII were excluded as they were observed by detectors with significant differences in response. The selection of regions enabled us to co-add as many spectra as possible. Thus we have obtained two sets (from the A and B pixels respectively) of co-added spectra from the three regions. This combined region has, following the convention in Table 2, $R_{\rm eff} = 3.8$ and a radius range (80% IPC flux) of 1.4–6.4. The co-added spectra had sufficient counts that the pulse height channels could be rebinned with a minimum of 25 counts per bin without sacrificing the spectral resolution from the instrument. The two sets of co-added spectra were simultaneously fitted with a Raymond & Smith (1977)[3] thermal plasma with a galactic absorption model (Morrison McCammon 1983). In the simultaneous fit, temperature, abun-

[3] We used the 1992, February version of their code.

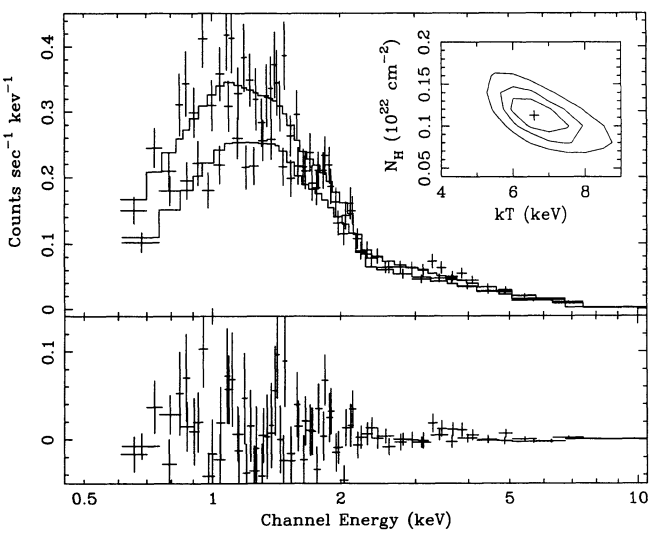

FIG. 3.—Two sets of pulse height spectra (from A and B pixels, respectively) for the combination of regions II, IV, and V are shown with the best-fit models to the simultaneous fit (Table 3) in the upper box. The residuals from the fit are shown in the lower box. Data points have 1 σ error bars. The spectra are binned for display. The vertical axes are in units of counts s^{-1} keV^{-1}. A confidence contour plot for gas temperature versus absorbing column density is shown near the upper right side corner of the spectrum. The contour values are $\Delta\chi^2 = 2.71$, 4.61, and 9.71.

dance (relative to cosmic[4]), and absorbing column density were jointly varied and normalizations were varied separately. The resulting best-fit values are listed in Table 3. The two sets of pulse height spectra and the best fit model are shown in Figure 3 along with residuals of the fit in the lower box. The spectra are rebinned for display. A confidence contour plot is shown for N_H (column density) versus kT (temperature) near the upper right corner of the figure. The temperatures of this region [$kT = 6.6\ (+1.1, -0.8)$ keV, 90% confidence errors] is consistent with the average temperature observed with *Ginga* ($kT = 7.7 \pm 0.2$ keV, Hatsukade 1989). The heavy-element abundance (0.4 ± 0.2), mainly determined by the strengths of Fe K and L lines in this fit, is also consistent with the Fe abundance deduced from the *Ginga* spectrum (Fe abundance $= 0.28 \pm 0.04$ cosmic, Hatsukade 1989), observed with a large field of view. The absorbing column density of $N_H = (1.1 \pm 0.3 \times 10^{21}$ cm^{-2} is not consistent with the galactic value from the 21 cm data ($N_H = 4.3 \times 10^{20}$ cm^{-2}) and an additional absorption component is needed, as in cooling flow clusters in the *Einstein* SSS data (White et al. 1991).

3.3. *Fit to Each Region*

Spectra from regions I–VII were fitted separately. The B4 pixel for region III was excluded from the analysis because the calibration for this particular pixel below 0.7 keV is unreliable, while the data between 0.6 and 0.7 keV are particularly important in constraining absorption parameters. We cannot assume the same spectra for the A2 and B4 pixels in region III because this particular region is sensitive to the slight offset between A and B pixels and in fact, our preliminary anaysis showed somewhat different temperatures in these pixels. In region VII, the A4 pixel was excluded from the analysis because it may be contaminated by electrical noise at low energies. Other than these, corresponding A and B pixels belonging to the same region were simultaneously fitted. In order to make use of the maximum-likelihood method (Cash 1979, hereafter ML-fit), since this method cannot be applied to the background-subtracted data, we have modeled the observed background. The background pulse height spectra selected for the observations (see § 3.1) were ML-fitted with one or two power laws. If significant residuals remain at the lowest energy channels (where a steep rise of the background is usually seen), a Gaussian was added to the background model. The pulse height spectra from the A2256 observations were binned such that each bin has a minimum of five counts. The binned and grouped spectra were then ML-fitted with the Raymond-Smith thermal plasma model with absorption plus the fixed background models for the corresponding spectra. As in § 3.2, all free parameters except the normalizations were jointly varied for simultaneous fits and normalizations were varied separately. For regions II, IV, V, VI, and VII, we used the model in § 3.2 with abundance fixed at 0.4 (§ 3.2) because the spectra for these regions were too poor to give reasonable constraints on the abundance. Table 4 summarizes the results of these fits. Spectra for regions I and III are treated in the next section. The source fluxes (0.8–10 keV) of the best-fit models are summarized in Table 6.

[4] Cosmic abundances of the elements considered in the Raymond-Smith model are from Allen (1973) except the iron abundance, which is from Ross & Aller (1976).

3.4. *Fit with an Edge Absorption Feature*

The spectra for region I and region III appear to show narrow absorption features around $E \sim 0.55$ keV, and we have tried to fit them with an absorption edge appropriate for the K-shell photoelectric absorption by oxygen (Tucker 1975). Spectra for other regions are truncated at 0.6 keV (last column in Table 4) and an absorption edge at $E_{ed} \sim 0.55$ keV and absorption by an extra column of neutral gas are essentially indistinguishable. In order to check the significance of the edge feature, we have made three fits to each of these regions: (i) Raymond-Smith with an absorption edge with plasma temperature, abundance, normalization(s), edge energy, and edge optical depth as free parameters. Absorption column density of the neutral gas was fixed to $N_H = 4.3 \times 10^{20}$ cm^{-2} (galactic value from the 21 cm data); (ii) no absorption edge and the absorbing column density is fixed to the galactic value, (iii) no absorption edge, N_H is a free parameter, i.e., allowing an excess absorbing column.

In both regions, fit (i) gave the best fit to the data. The source fluxes in Table 6 for regions I and III are for case (i) models. The result of these fits are summarized in Table 5 with the increase of the likelihood function from case (i). Figure 4 shows the 0.4–1.2 keV pulse height data for regions I (for the A0 pixel)

TABLE 4

FITS TO EACH REGION—1

REGION	kT (keV)	N_H (10^{20} cm^{-2})	NORMALIZATION[a] A	B (10^{12} cm^{-5})	B'	ENERGY RANGE (keV)
II	$7.4(+1.8; -1.3)$	$9. \pm 3.$	$3.57(+0.32; -0.29)$	$2.95(+0.23; -0.22)$	...	0.6–10
IV	$6.4(+1.3; -1.0)$	$11. \pm 3.$	1.69 ± 0.11	1.64 ± 0.11	...	0.6–10
V	$6.6(+1.4; -0.9)$	$11. \pm 3.$	3.94 ± 0.28	3.16 ± 0.22	...	0.6–10
VI	$7.9(+3.7; -2.2)$	$12. \pm 6.$	$0.44(+0.07; -0.06)$	0.32 ± 0.04	...	0.6–10
VII	$6.8(+2.3; -1.4)$	$16. \pm 6.$	0.97 ± 0.12	0.74 ± 0.09	0.94 ± 0.10	0.8–10

NOTES.—Abundance is fixed to 0.4 (cosmic = 1); 90% confidnece errors.

[a] The normalization is

$$\text{Normalization} = \frac{10^{-12}}{4\pi d^2} \int n_e^2\, dV\ ,$$

where d is the distance to the cluster. For region VII, three pixels were simultaneously fit and columns under A, B, and B' are normalizations for A3, B1, & B1 pixels, respectively. For other regions, columns under A and B are for A and B pixels for the corresponding region.

TABLE 5

FITS TO EACH REGION—2 (with an absorption edge)

REGION	MODEL	kT (keV)	ABUNDANCE (cosmic = 1)	ABSORPTION[a] E_{ed} (keV)	ABSORPTION[a] τ_{ed}	ABSORPTION[a] N_H (10^{20} cm^{-2})	NORMALIZATION[b] A (10^{12} cm^{-5})	NORMALIZATION[b] B (10^{12} cm^{-5})	Δ LIKELIHOOD OVER BEST-FIT MODEL	ENERGY RANGE (keV)
I	(i).....	7.7(+1.9; −1.5)	0.5 ± 0.3	0.55(+0.05; −0.12)	0.94(+0.44; −0.42)	4.3	1.18(+0.10; −0.15)	0.99(+0.08; −0.09)	0.	0.4–10.
	(ii).....	9.9(+3.3; −1.4)	0.6 ± 0.3	...	0.	4.3	1.06(+0.09; −0.11)	0.91(0.07; −0.08)	9.6	0.4–10.
	(iii).....	7.6(+2.0; −1.4)	0.5 ± 0.3	...	0.	11. ± 3.	1.20(+0.09; −0.17)	1.00(+0.09; −0.08)	2.8	0.4–10.
III	(i).....	4.6(+0.9; −0.7)	<0.3	0.58 ± 0.04	1.9 ± 0.5	4.3	2.40 ± 0.36	...	0.	0.5–10.
	(ii).....	8.4(+3.0; −1.0)	<0.3	...	0.	4.3	1.84(+0.11; −0.13)	...	23.	0.5–10.
	(iii).....	5.2 ± 1.2	<0.3	...	0.	19. ± 3	2.2 ± 0.3	...	7.2	0.5–10.

NOTES.—90% confidence errors and upper limits.

[a] Values without errors are fixed parameters.

[b] See the note under Table 4 for the definition of the normalization.

TABLE 6

X-RAY FLUXES

REGION	0.8–10 keV FLUX (10^{-11} ergs s^{-1} cm^{-2}) A	B	B′
I.....	$1.51(+0.13; -0.19)$	1.27 ± 0.11	...
II.....	$4.69(+0.42; -0.38)$	3.87 ± 0.30	...
III.....	2.10 ± 0.32	...	...
IV.....	1.97 ± 0.13	1.94 ± 0.13	...
V.....	4.96 ± 0.35	3.97 ± 0.27	...
VI.....	0.55 ± 0.08	0.40 ± 0.05	...
VII.....	1.14 ± 0.14	0.87 ± 0.11	1.11 ± 0.12

NOTE.—90% confidence errors. See the note under Table 4 for the defintions of A, B, & B′.

and III along with best-fit models for cases (i), (ii), and (iii) (*solid dashed*, and *dot-dashed lines*, respectively). Also shown are the corresponding background pulseheight spectra and their models. Although only the pulse height spectrum for the A0 pixel is displayed for region I in Figure 4, models are for simultaneous fits to A0 and B0 pixels. Looking at the model (ii) curves in Figures 4*a*, *b* (*dashed lines*) and pulse height data, one can see that a rather narrow absorption feature may fit the spectra. As shown in Table 5, fit (i) with the absorption edge improves the likelihood from the fit (ii) by 9.6 and 24 (for two additional free parameters) for regions I and III respectively and also gives a better fit than those with just additional column density. The residuals from fit (i) are not more than about 2 σ for any data point. However, there seems to be a common feature in the residuals from model (i) in both regions

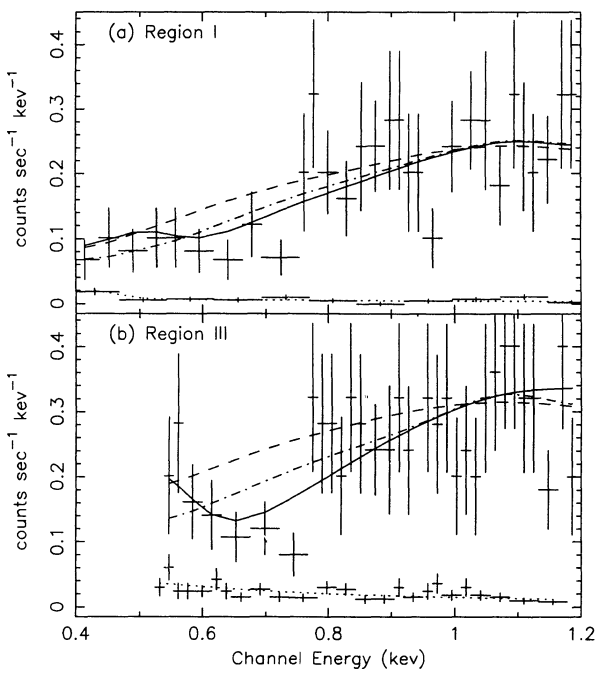

FIG. 4.—Pulse height spectra in the low energies (0.4–1.2 keV) for regions I (for the A0 pixel) and III are shown with the three models in Table 5. Solid, dashed, and dash-dotted lines are for models (i), (ii), and (iii) respectively. Also shown with these spectra are background pulse height spectra and their models (dotted lines, used for the ML fit) to demonstrate that their effect on the significance of the detection of the absorption edge is small.

I and III, i.e., a low count rate data point at $E \sim 0.74$ keV followed by a steep rise. We have failed to fit this feature with a narrow emission line because the spectral resolution of the instrument at this energy is not as sharp as this steep rise. A possible explanation is that some electrical noise preferentially contaminates channels corresponding to $\sim$0.78 keV. If so, the significance of the edge feature would be strengthened. Because this 0.78 keV feature is statistically weak, we do not discuss it any further. While differences in likelihood function values between (i) and (iii) are only marginally significant, there is another possible indication that the feature is likely to be an absorption edge rather than an additional column of neutral absorber. The *ROSAT* PSPC spectrum of the cool clump (B91), which is mostly in region III, shows no additional absorption in excess of the galactic value around 0.2–0.3 keV, where an absorption column of $N_H \sim 1 \times 10^{21}$ cm^{-2} would make a strong attenuation unless there is an additional soft component dominating this spectral range.

3.5. *Temperature and Abundance Distribution*

Region III has a significantly lower temperature [$T = 4.6\ (+0.9, -0.7)$ keV] than other regions in the cluster. This region contains the general area of the cool clump found by Briel et al. (1991) in the *ROSAT* PSPC data and is likely to be composed of two temperature components. Unfortunately with only about 1600 s of BBXRT exposure in this region, we were not able to resolve the spectrum into two temperature components. Other than this, there is no evidence for temperature differences among regions.

Abundances of region I (0.5 ± 0.3) covering the inner 3′ of the main body center, and the combined inner region ($R_{\rm eff} =$ 3.′8, covering 1.′4–6.′4 from the center) (0.4 ± 0.2) are both consistent with the value from the *Ginga* data (0.28 ± 0.04) with its large FOV (1° × 1.°8 FWHM) covering the entire cluster ($R_{\rm eff} \sim 7'$).

4. SPATIAL ANALYSIS

4.1. *The Emission Measure Profile*

Regions I, V, VI, and VII cover various parts of the main body without significant contamination by the cool clump. We have tried fitting the observed emission integrals from these regions with the usual spherically symmetric modified King profile, $S(\xi) = S(0)(1 + \xi^2/a^2)^{-3\beta+1/2}$, where a is the core radius and ξ is the projected radius (e.g., Jones & Forman 1984), centered at the main body peak (eastern peak of the *ROSAT* PSPC image). Out of nine normalizations from these regions, we made five data points by adding four pairs of normalizations from corresponding A and B pixels. These five data points were compared with the model emission measure accumulated over the sky covered by the pixels. Because of the small number of the spatial data points, we were not able to constrain both a and β but could constrain only a combination of these two. For the core radius of 4.′83 $\pm$ 0.′17 obtained from the *ROSAT* PSPC image (B91), our data show $\beta = 0.66 \pm 0.05$ (error corresponds to a χ^2 change of 2.7 for the range of core radius given above) giving $\chi^2 = 3.7$ for 2 degrees of freedom, which is somewhat smaller than their value ($\beta = 0.756 \pm 0.013$, 68% confidence level for three interesting parameters). The discrepancy may have come from the difference between fits to the unevenly sampled BBXRT data versus the azimuthally averaged profile of the PSPC image.

4.2. *Temperature Profile and Total Binding Mass*

4.2.1. *Mass Determination*

The variation of Raymond-Smith emissivity over temperatures from 5 to 10 keV, folded into the BBXRT effective area curve, is about ~5% and therefore we can consider the fitted emission integral with a single temperature good to a few percent even in an extreme case where temperature varies along the line of sight over 5–10 keV without a single dominant temperature component. Thus we can express the X-ray emitting gas density profile for the modified King brightness (emission measure) profile:

$$\rho_g(r) = \rho_g(0)\left(1 + \frac{r^2}{a^2}\right)^{-(3/2)\beta}, \quad (1)$$

without further correction (e.g., Cowie, Henriksen, & Mushotzky 1987, hereafter CHM). The central electron density derived from our surface brightness fit was $n_0 = (2.55 \pm 0.11) \times 10^{-3}\ h_{50}^{1/2}\ \mathrm{cm}^{-3}$ (the error corresponds to the range of β from the fit to the BBXRT data given in the previous section), in agreement with the value derived from the PSPC image [$n_0 = (2.55 \pm 0.12) \times 10^{-3}\ h_{50}^{1/2}\ \mathrm{cm}^{-3}$, Henry, Briel, & Nulsen 1993, 68% confidence error for three interesting parameters]. The mass of the X-ray emitting gas within a radius r can be estimated by integrating equation (1) over the volume of interest. This can be compared with the total gravitational mass over the same volume estimated using the expression

$$M_{\mathrm{grav}}(<r) = -\left(\frac{kT_g}{G\mu m_{\mathrm{H}}}\right)\left(\frac{d\log \rho_g}{d\log r} + \frac{d\log T_g}{d\log r}\right)r \quad (2)$$

(e.g., CHM). While the first term can be evaluated using equation (2), additional information, i.e., spatially resolved temperature information, is needed to evaluate the second term. In the following sections, we explore possible mass distributions consistent with the BBXRT spectral data from regions I, V, VI, and VII. Although it would have been better to predict the pulse height spectra for each region from the models and fit to the pulse height data directly to constrain model parameters, applying such a procedure to the BBXRT data analyzed here requires an impractically large computational load and would not be of any benefit given the signal-to-noise ratio of our data. Instead, we have compared the emissivity averaged mean temperatures over the regions predicted from the model with the fitted temperatures from the observed spectra.

4.2.3. *Polytropic Model*

First, we assumed a polytropic equation of state, [$T_g(r) \propto \rho_g^{\gamma-1}$] for the gas. Using equation (1), the emissivity (roughly $\propto \rho_g^2$) weighted average temperature along a line of sight at a projected distance ξ from the center $T_p(\xi)$ is

$$T_p(\xi) = \frac{\int T_g(r)\rho_g(r)^2\, dl}{\int \rho_g(r)^2\, dl} = T_p(0)\left(1 + \frac{\xi^2}{a^2}\right)^{-[3\beta(\gamma-1)/2]}, \quad (3)$$

where $r^2 = \xi^2 + l^2$. This projected temperature was averaged separately over regions I, V, VI, and VII weighted by the emission measure eq. [1]) and compared with the data. If we use $(a, \beta) = (4'.8, 0.756)$ from the PSPC image, we obtained $\gamma = 1.10 \pm 0.35$ (90% confidence error). We have obtained essentially the same result for $\beta = 0.66$ (best-fit to the BBXRT data). For the polytropic case, the total binding mass of A2256 is

$$M_{\mathrm{grav}}(\le r) \approx 8.0 \times 10^{13}\left(\frac{kT_g}{7\ \mathrm{keV}}\right)\beta\gamma \times \left[1 + \left(\frac{r}{a}\right)^2\right]^{-1}\left(\frac{r}{a}\right)^2 r'[\mathrm{arcmin}]h_{50}^{-1}\ M_\odot, \quad (4)$$

where r' is the angular scale corresponding to r at the distance of A2256. At $r = 8'$ [a reasonable BBXRT coverage limit (0.8 h_{50}^{-1} Mpc)], the allowed range of gravitational mass for the polytropic model is $M_{\mathrm{grav}}(r \le 8') = (3.0\text{–}3.8) \times 10^{14}\ h_{50}^{-1}\ M_\odot$.

4.2.3. *Other Mass Models*

The alternative approach we consider utilizes a fairly general parameterization of the mass distribution to derive temperature profiles from the equation of hydrostatic equilibrium (eq. [2]). The model projected temperature profiles were averaged over regions and compared with the BBXRT temperature data as before. This approach is complementary to those using the polytropic assumption or other assumptions about the temperature profile to infer the mass profile.

The mass distribution we consider consists of the following three components: (*a*) a hot gas component, (*b*) a component proportional to the distribution of the galaxy light, and (*c*) a (nonluminous) component with a core and an r^{-2} density profile at large radii:

$$\rho = \rho_{\mathrm{gas}} + A\left(1 + \frac{r^2}{a_{\mathrm{light}}^2}\right)^{-3/2} + B\left(1 + \frac{r^2}{a_{\mathrm{dark}}^2}\right)^{-1}. \quad (5)$$

The constants A, B, and a_{dark} are the parameters of the model and ρ_{gas} is from the PSPC imaging data. The second term is approximately proportional to the galactic luminosity density, and a galaxy core radius of $a_{\mathrm{light}} = 7'.8$ was used as a convenient representation of the galaxy surface density of the main body (Fabricant et al. 1989; Henry et al. 1992). In practice, we consider only models where either the second or third component is negligible. Therefore we assume that the dark matter is either proportional to the light or is distributed as an isothermal sphere; more general parameterizations are not warranted by the limited number and accuracy of the temperature measurements. Acceptable models can be found for a wide range of the above parameters, including those where the dark matter is proportional to the cluster light, models where a_{dark} is equal to or slightly greater than a_{light}, and models where a_{dark} is one-tenth of a_{light}.

It is not surprising that the detailed, small-scale distribution of matter cannot be constrained by the BBXRT data with its crude spatial resolution. However, the integrated mass out to 0.8 Mpc ($\approx 8'$) is very similar among the best-fit models. We consider models with the deviation of the likelihood function from the best-fit model smaller than 2.7 for each class ($B = 0$ with varying A, or a_{dark} = constant with varying B) and no single temperature data point (out of four) is more than 2 σ away from the model as acceptable. In this case, the total range of acceptable models have $M_{\mathrm{grav}}(<8') \approx (2.8\text{–}3.3) \times 10^{14}\ M_\odot$. This agrees well with the estimates derived above using the polytropic model.

4.2.4. *Mass Profiles*

Figure 5 shows the enclosed gravitational mass as a function of radius for the best-fit gamma ($\gamma = 1.10$) model and models giving the largest and smallest gravitational masses at $r = 8'$. Figure 5 also shows the mass of the X-ray emitting gas and its

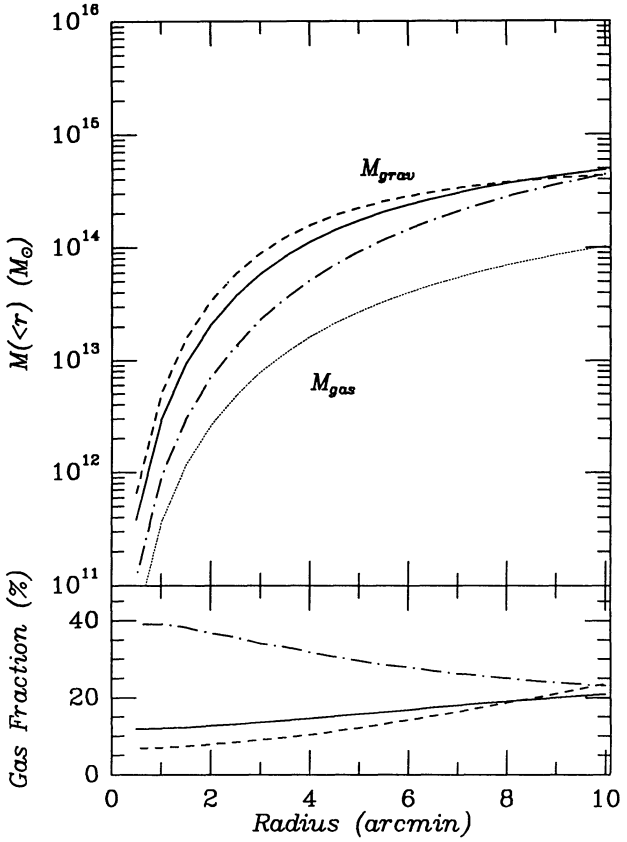

FIG. 5.—Radially integrated mass profiles are shown for X-ray emitting gas (*dotted line*) and the total gravitational mass for the best-fit γ model ($\gamma = 1.10$; *solid line*) and models giving maximum mass (*dashed line*) and minimum (*dot-dashed line*) masses within $r = 8'$. The gas fraction of the total gravitational mass is also plotted with the same line styles as corresponding total mass models. One arcmin roughly corresponds to 0.1 h_{50}^{-1} Mpc. These mass estimates also scale with the Hubble constant. See text.

fraction of the gravitational mass. The total gas mass scales with the Hubble constant as $h_{50}^{-5/2}$, while M_{grav} scales as h_{50}^{-1} and is proportional to the gas temperature. The gas fraction scales, therefore, as $h_{50}^{-3/2}$. Figure 6 shows the projected temperature profiles for these models with the temperature data from BBXRT. Figure 5 shows that the behavior of the total gravitational mass diverges for acceptable models at $r \leq 5'$ (0.5 h_{50}^{-1} Mpc) but is insensitive to the choice of models around $r \sim 8$–$10'$ (0.8–1.0 h_{50}^{-1} Mpc).

5. DISCUSSION

5.1. *Nature of the Absorbing Material*

The detected absorption edges (§ 3.4) in regions I and III at $E_{edge} \sim 0.5$–0.6 keV are most likely due to K-shell photoionization of oxygen (Tucker 1975; Reilman & Manson 1979). There was no indication of an accumulation of ice on the BBXRT detectors, which could have created a similar absorption feature, during the mission (Weaver 1993). The K-shell absorption cross section at $E_{edge}(\sigma_{edge})$ is insensitive to the ionization stage of oxygen and $\sigma_{edge} \sim 5 \times 10^{-19}$ cm^2. Assuming that the absorber is distributed over the sold angle covered by the pixel (~ 10 and 40 arcmin^2 for regions I & III respectively), a threshold optical depth $\tau_{edge} \sim 0.5$–1.4 for region I implies an amount of absorbing gas of 1–$3 \times 10^{12}[\mathrm{O/H}]^{-1}\ h_{50}^{-2}\ M_\odot$, where [O/H] is the ratio of oxygen to hydrogen relative to the cosmic value. A similar assumption leads to an estimate of 1–$3 \times 10^{13}[\mathrm{O/H}]^{-1}\ h_{50}^{-2}\ M_\odot$ of absorbing gas in region III. These estimates are, especially in region III, quite dependent on the geometry of the absorbing material. One overestimates the quantities if the absorbing gas preferentially lies along the line of sight of the brighter part on the pixels and underestimates them if gas is scattered over the volume occupied by the X-ray emitting gas.

The 90% confidence range of E_{edge} implies that oxygen is at ionization stages no higher than O^{5+} in region I and between O^{2+} and O^{5+} in region III at the redshift of A2256. Although BBXRT data alone cannot exclude the possibility that there is significant absorption by neutral or once-ionized helium, the fact that the *ROSAT* PSPC spectrum of the cool clump does not show any sign of deep absorption at ~ 0.2 keV (B91) is a possible indication that helium in the absorbing gas is almost completely ionized, at least in region III, unless there is an additional soft component dominating the 0.2–0.3 keV band which does not affect the spectra above ~ 0.4 keV. While such a possibility cannot be fully excluded, we here discuss possible scenarios assuming that the helium in the absorbing gas is almost fully ionized.

Time-dependent cooling calculations beginning with 10^6 K equilibrium gas by Shapiro & Moore (1976) show the fraction of elements at various stages of ionization versus gas temperature. Comparing their calculations (time-dependent rather than steady state) with the above ionization ranges, the temperature of the absorbing gas is in the range 0.5–2×10^5 K. A higher temperature ($\sim 5 \times 10^5$ K) is required in the case of equilibrium. If collisional ionization is supplemented by photoionization, the desired ionization configuration could be attained with a lower temperature. For a gas cloud with a cosmic O/H ratio, the observed optical depths of the oxygen edges imply a thickness of the absorber of about $1 n_H^{-1}$ kpc where n_H is in cm^{-3}. If the absorbing gas is composed of numerous small blobs, the upper limit of the radius of each blob r can be set by requiring that the covering fraction by clouds over the cooling region exceeds unity (White et al.

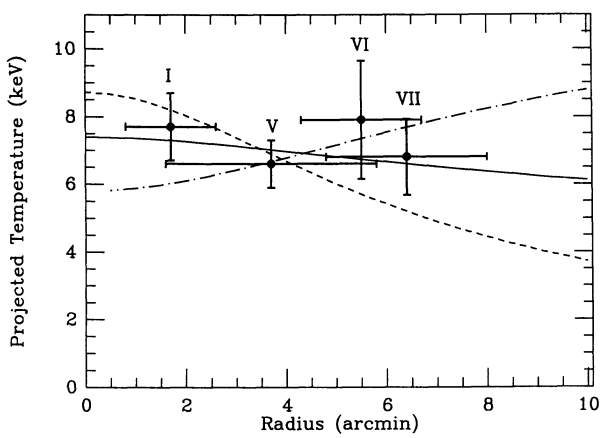

FIG. 6.—Fitted temperatures of the regions used in the spatial analysis are plotted as a function of approximate radius from the center. Names of the regions are indicated just above the data points. Vertical error bars represent 1 σ errors. Nominal radii and horizontal error bars represent the means and standard deviations of the distance from the main body center weighted by the model brightness profile for corresponding regions. Projected temperature profiles for the models shown in Fig. 5 are plotted with the same line styles as Fig. 5.

1991):

$$\frac{r}{R} \leq \frac{M}{4n_{\rm H} m_{\rm H} R^3} \cong \frac{N_{\rm H}}{n_{\rm H} R} . \quad (6)$$

This condition is equivalent to the statement that r must be smaller than the thickness of the absorbing material estimated above, i.e., $r \lesssim 1 n_{\rm H}^{-1}$ kpc. If the absorbing material came from the X-ray emitting hot gas in the process of cooling, blobs can be formed through thermal and/or kinetic instabilities. Each blob cools, keeping pressure equilibrium with the surrounding gas, until its sound crossing time excceds its cooling time at $T \sim 3 \times 10^6 r^{0.32}$ K, where r is in kpc. After that point, it cools isochorically down to 10^4 K. Then repressurization occurs suddenly through shock waves which heats up the blob to 10^5 K again (Fabian, Nulsen, & Canizares 1984). The reheated gas emits UV photons, providing the surrounding gas with ionizing radiation, and cools rapidly. In a blob with $r \lesssim 1 n_{\rm H}^{-1}$ kpc surrounded by the diffuse intracluster gas in A2256 with $T \sim 10^8$ K and $n_{\rm H} \sim 10^{-3}$ cm^{-3}, the transition from isobaric to isochoric cooling occurs at $T \lesssim 10^7$ K and $n_{\rm H} \gtrsim 10^{-2}$ cm^{-3}. Then, the cooling timescale at $T \sim 10^5$ K is $\sim 10^5 n_{\rm H}^{-1} \lesssim 10^7$ yr (Shapiro & Moore 1976). If a significant fraction of the intracluster gas ($\sim 10^{13}$ $M_\odot$) goes through this cooling process during the whole phenomenon, there could be ~ 10 generations of 10^{12} $M_\odot$ of gas at $T \sim 10^5$ K over $\sim 10^8$ yr. Existence of additional ionizing sources can make this time scale longer. The completely cooled gas may have turned into stars or smaller blobs, preventing us from detecting X-ray absorption by neutral gas, at least in region III. In turn, the absorbing gas may have been heated up from the colder gas as discussed in § 5.3. The following sections discuss two possible origins of this absorbing material.

5.2. *A "Merger-driven Shock Waves" Picture*

We have considered the possibility that the origin of the "warm" absorbing gas is due to post-shock cooling following shock waves driven by merging of the subcluster into the main body of A2256. The systematic velocity difference of galaxies in the two bodies of the cluster is ~ 2100 km s^{-1} (B91). If the relative velocity of main body and subcluster gases was initially about this speed, the collision is mildly supersonic [$c_a = (5kT/3\ \mu m_{\rm H})^{-1/2} \sim 1400$ km s^{-1} in the main body and ~ 700 km s^{-1} in the subcluster]. As Fabian & Daines (1991) discussed, the ram pressure of the collision is comparable to the thermal pressure of the intracluster gas of both the main body and the subcluster. Therefore the generation of shock waves is marginal. If shock waves were generated, those could compress and heat intracluster gas which would subsequently cool because of the increased cooling rate by the compression. A similar scenario is suggested to explain absorption in the *ROSAT* images of supernova remnants (Aschenbach 1992).

In order to assess such a possibility in the environment of A2256, we have calculated the timescale needed for the shock-heated subcluster gas to cool to 10^7 K for shock velocities of 800–3000 km s^{-1}. For the calculation, we have assumed the temperature of the preshock gas is $kT = 2$ keV (B91) and the electron density of $n_e = 5 \times 10^{-3}$ cm^{-3} (Fabian & Daines [1991], at ~ 100 kpc away from the subcluster center). After crossing the shock front adiabatically, the postshock gas is assumed to cool isobarically to 10^7 K. The cooling rate per unit mass inferred from the Raymond-Smith thermal plasma model for the heavy-element abundance of 0.4 (Table 2) is $\Lambda(n_e, T) \sim 5.0$ $[kT(\text{keV})]^{0.4}$ $[n_e(\text{cm}^{-3})]$ ergs s^{-1} g^{-1} for $1.5 \lesssim kT(\text{keV}) \lesssim 10$ $[1.7 \times 10^7 \lesssim T(\text{K}) \lesssim 1.2 \times 10^8]$ and $\Lambda(n_e, T) \sim 7.0$ $[kT(\text{keV})]^{-0.4}$ $[n_e\ (\text{cm}^{-3})]$ ergs s^{-1} g^{-1} for $0.8 \lesssim kT(\text{keV}) \lesssim 1.5$ $[1 \times 10^7 \lesssim T(\text{K}) \lesssim 1.7 \times 10^7]$. The resulting cooling time $t_{\rm cool}(\text{shock} \rightarrow 10^7\ \text{K})$ is plotted against the shock speed in Figure 7. Figure 7 shows that it takes at least 4.5×10^9 yr for the shocked gas to cool to 10^7 K, which is several times longer than the crossing time of the subcluster through the main body ($\sim 1 \times 10^9$ yr). If milder shock waves have been generated in the main body gas, the cooling time of their postshock gas is still longer, because it has higher initial temperature and compression is weaker. As a result, the post-shock cooling is unlikely to generate the large amount of warm absorbing gas observed.

5.3. *A "Cooling Flow" Picture*

Another possibility is that the absorbing gas originates in the cooling flow contained in the subcluster. Fabian & Daines (1991) showed that the subcluster may well have contained a cooling flow based on its inferred density from the *ROSAT* PSPC image by B91, while the main body is unlikely to contain or to ever have contained one. The amount of cold material detected in the *Einstein* SSS spectra (White et al. 1991) as extra absorption in some cooling flow clusters is typically 10^{12}–10^{13} $M_\odot$. This is comparable to the amount of the ionized absorbing material in A2256. Since they analyzed spectra only above 0.6 keV, their observations do not exclude the possibility that some of the extra absorption in their sample is due to partially ionized oxygen rather than cold neutral gas. In turn, the existence of the warm absorbing gas may be a phenomenon specific to A2256, indicative of an extraordinary property of the intracluster environment in A2256, as Bridle et al. (1979) noted based on the unusual abundance of head-tail radio sources of the region. It may be natural to search for the origin of these unusual properties in the merging of the subcluster. One of the possible pictures is that cold gas similar to that seen in ordinary cooling-flow clusters was shock-heated up to $\sim 10^7$ K by the effects of merging followed by a radiative cooling to $\sim 10^5$ K. While gas is cooling, processes described in § 5.1 occur. It is also possible that there are ionizing radiation sources such as required to explain emission-line nebulosities seen in the central region of

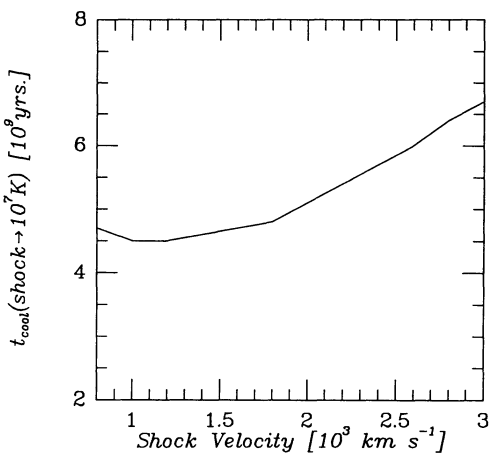

FIG. 7.—Cooling time for post-shock gas to cool to 10^7 K is plotted vs. shock speed for preshock gas of $kT = 2$ keV, $n_e = 5 \times 10^{-3}$ cm^{-3} and a heavy element abundance of 0.4 of the cosmic value.

cooling-flow clusters (Crawford & Fabian 1992). Active galactic nuclei in the centers of the several head-tail radio sources in the map of Bridle et al. (1979) and Bridle & Fomalont (1976) are possible sources of the ionizing radiation.

5.4. *Implications for Observations in Other Wavelengths*

If there is a significant amount of gas at temperatures ranging from 10^4 to 10^6 K, there should be a significant amount of emission on the optical–UV range. A calculation by Netzer (1992) of a 10^5 K gas shows that the luminosity of the optical continuum between 3000 Å and 7000 Å is about $2 \times 10^{45}(M/10^{12}\ M_\odot)n_H$ ergs s^{-1}. A strong Hα line is expected with a luminosity 5 times larger than the continuum. Partridge (1990) and colleagues reported a detection of diffuse optical emission in A2256 in their CCD images in the *r*, *i*, and *V* bands. The total luminosity of all these bands they have detected was $\sim 2 \times 10^{45}$ ergs s^{-1}. This order of magnitude coincidence may indicate that the diffuse optical emission they have detected may have come from the gas responsible for the absorption seen by BBXRT. In view of this, it would be interesting to make CCD observations through a narrow-band filter centered at the redshifted Hα. A narrow-band image is also important to find possible ionizing sources. It may be possible to detect or set limits on the amount of neutral absorbing material along several lines of sight by observing H I absorption against the radio sources detected by Bridle & Fomalont (1976) (also Bridle et al. 1979).

5.5. *Mass Profile and Dark Matter Content*

Figure 5 shows that the X-ray emitting gas accounts for $\sim 0.2\ h_{50}^{-3/2}$ of the total cluster mass within 10′ (1.0 h_{50}^{-1} Mpc). This value is insensitive to the models consistent with our temperature constraints as discussed in § 4.2.2 and 4.2.3. The total mass contained in the member galaxies is hard to estimate because of the uncertainties at the low end of the luminosity function below the survey limit by Fabricant et al. (1989). The Coma Cluster, which has properties similar to A2256, as discussed below, is about 2.5 times closer than A2256 and provides a better estimate of the galaxy content of the mass profile. According to Figure 9 of Watt et al. (1992) for the Coma Cluster, the mass density of the galaxies accounts for about 5% of the total gravitational mass density and this ratio does not vary rapidly with radius. If this ratio also applies to A2256, about 75% ($h_{50} = 1$) of the total mass within 1 Mpc (10′) is in the form of dark matter.

Watt et al. (1992) showed, based on their observation of the Coma Cluster using the Spacelab 2 XRT, that the temperature profile of Coma is consistent with an isothermal distribution for the inner 1 Mpc of the cluster. They have derived a gravitational mass of Coma within 1 Mpc from the center of 4.2–5.2 $\times 10^{15}\ M_\odot$ (see also Hughes 1989). This is similar to the total gravitational mass of A2256 within the same volume (Fig. 5). As noted by Fabricant et al. (1989), Coma and A2256 are similar in various ways. They are both rich clusters of type B in the R-S classification (Rood & Sastry 1971), i.e., there are two dominant galaxies near the center. They both have rather smooth, relaxed X-ray profiles with similar overall gas temperatures of 7–8 keV. The lack of cooling flow structures is also common to both. Substructures become apparent in higher spatial resolution images of both clusters (Davis & Mushotzky 1993; B91; Briel, Henry, & Böhringer 1992). The substructure in A2256, however, appears more prominent. The BBXRT observation of A2256 and the Spacelab 2 XRT observation of Coma show that they are also similar in total mass and gas fraction within central 1 Mpc. It may be interesting to view these two similar clusters under the hypothesis that they were formed by subsequent mergings of smaller clusters to the main body and/or a major merging of two approximately equal-mass clusters. These mergings may have washed out the preexisting structures on a timescale of $\sim 10^9$ yr ($\sim$ sound crossing time). Another merging of a smaller cluster takes place subsequently. Coma and A2256 may be two slightly different snapshots of essentially the same phenomena.

6. CONCLUSIONS

The cluster of galaxies A2256 was observed with BBXRT for a total exposure of about 4000 s. Growing evidence exists that this cluster is an undergoing merger of two clusters. With rough positional sensitivity and medium spectral resolution, our BBXRT observations verified the existence of the cool clump detected by *ROSAT*. It revealed extra absorption over the cluster. In some locations of the cluster, an edge feature corresponding to K-shell photolectric absorption was apparent in the spectra. In one location, the absorption edge energy is consistent with partially ionized, rather than neutral, oxygen indicating that a large amount ($\sim 10^{12}$–$10^{13}\ M_\odot$) of ionized absorbing material with $T \sim 0.5$–5×10^5 K exists. It is unusual that such a large amount of gas exist at these temperatures because its cooling timescale is very short. However, considering that the blobs of the absorbing gas are likely to cool isochorically, they can stay at this temperature range for $\sim 10^7$ yr and there may be several generations of cooled gas. Postshock compression of the intracluster gas by shock waves caused by the merging is not likely to initiate cooling of the intracluster gas to generate this warm absorbing gas, because the cooling timescale of the postshock gas is still too long. It may have its origin in the cold gas contained in the subcluster cooling flow, heated by shock waves and/or ionized by radiation sources.

With spatially resolved spectroscopy, we have constrained the radial temperature gradient of the main body corresponding to the polytropic index $\gamma = 1.10 \pm 0.35$. Alternatively, we have also considered a range of models of the mass distribution in A2256 to compare with the spatially resolved temperature data from BBXRT. The total gravitational mass within 8′ (0.8 h_{50}^{-1} Mpc) of the cluster center is $M_{\rm grav}(\leq 8') = (2.8$–$3.7) \times 10^{14}\ M_\odot$ for the models consistent with our data.

About a month after submitting the first version of this paper, we received a preprint by Henry, Briel, & Nulsen reporting the mass determination analysis of the *ROSAT* PSPC image of A2256. Their conclusions about temperature gradient and mass of the cluster are essentially the same as ours.

We appreciate the prelaunch and postlaunch efforts of all the personnel which have lead to the successful completion of the BBXRT mission. We thank Hagai Netzer for calculating the warm gas spectra in the optical–UV region, and Bruce Partridge for the correspondence about the diffuse optical emission.

REFERENCES

Allen, C. W. 1973, Astrophysical Quantities (3d ed.; London: Athlone)
Aschenbach, B. 1992, preprint
Beers, T. C., & Geller, M. J. 1983, ApJ, 274, 491
Böhringer, H., Schwarz, R. A., Briel, U. G., Voges, W., Ebeling, H., Hartner, G., & Cruddace, R. G. 1992 in Clusters and Superclusters of Galaxies, ed. A. C. Fabian (Dordrecht: Kluwer), 72
Bridle, A. H., & Fomalont, E. B. 1976, A&A, 52, 107
Bridle, A. H., Fomalont, E. B., Miley, G. K., & Valentijn, E. A. 1979, A&A, 80, 201
Briel, U. G., et al. 1991, A&A, 246, L10 (B91)
Briel, U. G., Henry, J. P., & Böhringer, H. 1992, A&A, 259, L31
Cash, W. 1979, ApJ, 228, 939
Cowie, L. L., Henriksen, M., & Mushotzky, R. F. 1987, ApJ, 317, 593 (CHM)
Crawford, C. S., & Fabian, A. C. 1992, MNRAS, 259, 265
Davis, D. S., & Mushotzky, R. F. 1993, AJ, 105, 409
Evrard, A. E. 1990a, ApJ, 363, 349
———. 1990b, in Clusters of Galaxies, ed. W. R. Oegerle, M. J. Fitchett, & L. Danly (Cambridge: Cambridge Univ. Press), 287
Fabian A. C., & Daines, S. J. 1991, MNRAS, 252, 17P
Fabian, A. C., Nulsen, P. J. E., & Canizares, C. R. 1984, Nature, 310, 733
Fabricant, D., & Gorenstein, P. 1983, ApJ, 267, 535
Fabricant, D. G., Kent, S. M., & Kurtz, M. J. 1989, ApJ, 336, 77
Fabricant, D., Rybicki, G., & Gorenstein, P. 1984, ApJ, 286, 186 (FRG)
Forman, W., & Jones, C. 1990, in Clusters of Galaxies ed. W. R. Oegerle, M. J. Fitchett, & L. Danly (Cambridge: Cambridge Univ. Press), 257
Geller, M. J., & Beers, T. C. 1982, PASP, 94, 421
Harris, D. E., et al. 1990, The *Einstein Observatory* Catalog of IPC X-Ray Sources (Cambridge: Smithsonian Institution Astrophysical Observatory)
Hatsukade, I. 1989, Ph.D. thesis, Osaka Univ.
Henry, J. P., Briel, U. G., & Nulsen, P. E. J. 1993, A&A, 271, 413
Hughes, J. 1989, ApJ, 337, 21
Jones, C., & Forman, W. 1984, ApJ, 276, 38
Matilsky, T., Jones, C., & Forman, W. 1985, ApJ, 291, 621
Morrison, A., & McCammon, D. 1983, ApJ, 270, 119
Netzer, H. 1992, private communication
Partridge, R. B. 1990, in IAU Symp. 159, in The Galactic and Extragalactic Background Radiation, ed. S. Bowyer & C. Leinert (Dordrecht: Kluwer), 283
Raymond, J. C., & Smith, B. W. 1977, ApJS, 35, 419
Reilman, R. F., & Manson, S. T. 1979, ApJS, 40, 815
Richstone, D., Loeb, A., & Turner, E. L. 1992, ApJ, 393, 477
Rood, H. I., & Sastry, G. N. 1971, PASP, 83, 313
Ross, J. E., & Aller, L. H. 1976, Science, 191, 1223
Schindler, S., & Müller, E. 1993, A&A, 272, 137
Serlemitsos, P., et al. 1992, in Frontiers in X-ray Astronomy, Proc. 28th Yamada Meeting, Nagoya, Japan, ed. Y. Tanaka & K. Koyama (Tokyo: Universal Academy Press)
Shafer, R. A., Haberl, F., & Arnaud, K. A. 1989, XSPEC; An X-ray Spectral Fitting Package (ESA TM-09) (Paris: ESA)
Shapiro, P. R., & Moore, R. T. 1976, ApJ, 207, 460
Thomas, P. A., & Couchman, H. M. P. 1992, MNRAS, 257, 11
Tucker, W. H. 1975, Radiation Processes in Astrophysics (Cambridge: MIT Press), 243
Watt, M. P., Ponman, T. J., Bertram, D., Eyles, C. J., Skinner, G. K., & Wilmore, A. P. 1992, MNRAS, 258, 738
Weaver, 1993, Ph.D. thesis, Univ. Maryland, in preparation
White, D. A., Fabian, A. C., Johnstone, R. M., Mushotzky, R. F., & Arnaud, K. A. 1991, MNRAS, 252, 72